Superconducting spin-valve effect in heterostructures with ferromagnetic Heusler alloy layers

A. A. Kamashev,[1,*] N. N. Garif'yanov,[1] A. A. Validov,[1] J. Schumann,[2] V. Kataev,[2] B. Büchner,[2,3] Ya. V. Fominov,[4,5,6] and I. A. Garifullin[1]

[1]*Zavoisky Physical-Technical Institute, FRC Kazan Scientific Center of RAS, 420029 Kazan, Russia*
[2]*Leibniz Institute for Solid State and Materials Research IFW Dresden, D-01069 Dresden, Germany*
[3]*Institute for Solid State and Materials Physics, Technical University Dresden, D-01069 Dresden, Germany*
[4]*L. D. Landau Institute for Theoretical Physics RAS, 142432 Chernogolovka, Russia*
[5]*Moscow Institute of Physics and Technology, 141700 Dolgoprudny, Russia*
[6]*National Research University Higher School of Economics, 101000 Moscow, Russia*

(Received 17 July 2019; revised manuscript received 3 October 2019; published 23 October 2019)

We report a comparative analysis and theoretical description of the superconducting properties of two spin-valve-valve structures containing the Heusler alloy $Co_2Cr_{1-x}Fe_xAl_y$ as one of two ferromagnetic (F1 or F2) layers of the F1/F2/S structure, where S stands for the superconducting Pb layer. In our experiments, we used the Heusler alloy layer in two roles: as a weak ferromagnet on the place of the F2 layer and as a half-metal on the place of the F1 layer. In the first case, we obtained a large ordinary superconducting spin-valve effect ΔT_c assisted by the triplet superconducting spin-valve effect $\Delta T_c^{\rm trip}$. In the second case, we observed a giant magnitude of $\Delta T_c^{\rm trip}$ reaching 0.5 K. An underlying theory based on the solution of the Usadel equations using Kupriyanov-Lukichev boundary conditions with arbitrary material parameters for all layers and arbitrary boundary parameters for all interfaces is presented in the Appendix. We find a good agreement between our experimental data and theoretical results.

DOI: 10.1103/PhysRevB.100.134511

I. INTRODUCTION

In the past two decades, there has been enormous theoretical and experimental interest in the development of the elements for superconducting (SC) spintronics (see, e.g., Refs. [1,2]). Among those works, studies of the superconductor/ferromagnet/superconductor (S/F/S) heterostructures were considered to be promising for their use in the elements of quantum logics [3]. An element of the quantum cubit [4,5] is based on the so-called Josephson π contact [6,7], which can be realized in the S/F/S thin film multilayer. In this respect, the S/F contact has attracted long-standing fundamental interest [8]. In particular, the possibility to build up a superconducting spin valve (SSV) based on the S/F proximity effect has been theoretically suggested by Oh *et al.* [9]. They proposed an F1/F2/S trilayer with the S layer placed on top of the two F layers, where magnetizations are decoupled. In this theory, the critical temperature T_c of the SC heterostructure for the antiparallel (AP) mutual orientation of magnetizations should be larger than for the parallel (P) one. This is because the mean exchange field from two F layers acting on the Cooper pairs in the S layer is smaller for the AP configuration as compared to the P case. An alternative structure F/S/F with a similar operational principle was proposed theoretically by Tagirov [10]. However, it took more than ten years before a full switching between the normal and the SC states of such a device was realized experimentally [11].

Importantly, Fominov *et al.* [12] have theoretically shown that the interference of the Cooper pairs wave function reflected from both surfaces of the F2 layer in the F1/F2/S structure may be constructive or destructive. It depends on the thickness of the F layer, yielding the direct and inverse SSV effects, respectively. Indeed, a thickness-dependent sign-changing oscillating behavior of the SSV was experimentally observed in Ref. [13]. Therefore, the initial assumption by Oh *et al.* [9] that the AP mutual orientation of magnetizations of the F1 and F2 layers is preferable for superconductivity may not be always correct.

Figure 1 shows schematically the operation of the SSV in its most simple version. The two SC transition curves with the width δT_c corresponding to the P and AP mutual orientation of the magnetizations of the F1 and F2 layers are shifted with respect to each other by $\Delta T_c = T_c^{\rm AP} - T_c^{\rm P}$ and enclose the operational area of the SSV depicted by the shaded rectangle. Here, $T_c^{\rm AP}$ and $T_c^{\rm P}$ are the SC transition temperatures for AP and P configurations, respectively. At a fixed temperature within this rectangle, the change of the mutual orientation of magnetizations from AP to P by an external magnetic field yields a full switching between the SC and the normal state of the SSV. Therefore, the width $\Delta T_c^{\rm full}$ of the shaded area in Fig. 1 is the most important parameter of the SSV. It should be noted that the commonly used condition for the realization of the full switching effect $\Delta T_c > \delta T_c$ is, in fact, not sufficient. The actually relevant parameter $\Delta T_c^{\rm full}$ is always smaller than ΔT_c due to the finite value of δT_c, and this difference gets larger the larger the value of δT_c. In the first experimental realization of the full switching between the normal and SC states in the SSV in Ref. [11], $\Delta T_c^{\rm full}$ was of the order of 10 mK, only. Thus, to improve the performance of the SSV, it is necessary to increase this temperature window

*Corresponding author: kamandi@mail.ru

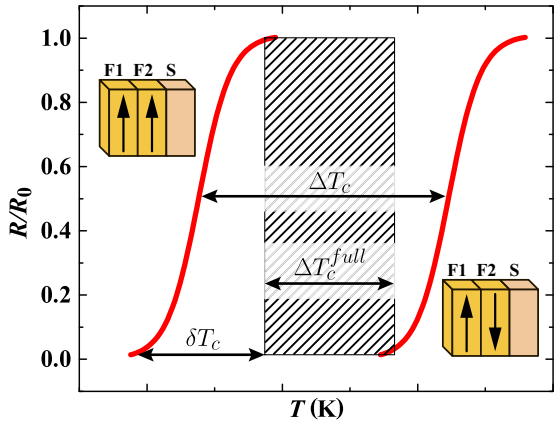

FIG. 1. Schematics of the operation principle of the SSV. SC transition curves (resistivity ratio R/R_0 as a function of T) with the width δT_c for the P ($\uparrow\uparrow$) and AP ($\uparrow\downarrow$) orientations of the magnetizations of the F1 and F2 layers are sketched by solid lines. Shaded rectangle depicts the operational area of the SSV (see the text).

which was attempted in a large number of works on different constructions of SSVs (see, e.g., reviews [14–16] and more recent publications [17–19]).

Recently, the studies of the SSV effect shifted toward exploring the long-range triplet component (LRTC) [20] in the SC condensate generated in heterostructures with noncollinear (close to orthogonal) orientations of the magnetizations of the F1 and F2 layers [12] (see also more recent articles [21–33]). For example, Jara *et al.* [34] have experimentally studied the SC properties of the CoO/Co/Cu/Co/Nb SSV structure. They obtained clear evidence for LRTC and good agreement between theory and experiment [35] (the theory of LRTC used in that paper was based on the numerical solution of the microscopic Bogoliubov – de Gennes equations). A full switching between the normal and SC states assisted by the triplet contribution to the SSV effect was observed by us in the CoO_x/Py1/Cu/Py2/Cu/Pb structure (Py = $Ni_{0.81}Fe_{0.19}$) [36]. The same result was obtained by Gu *et al.* [37,38] who studied epitaxial Ho/Nb/Ho and Dy/Nb/Dy SSV structures. They found the magnitude of the SSV effect of ∼400 mK.

At present, practically all fundamental questions of the SSV effect seem to be well understood and it comes out that the magnitude of the SSV effect in the constructions with elemental ferromagnets can hardly be increased anymore, calling for the use of new unconventional ferromagnetic materials. Singh *et al.* [39] successfully used a half-metallic CrO_2 layer as the F1 layer in the F1/Cu/F2/S structure. They obtained a giant magnitude of the triplet SSV effect in CrO_2/Cu/Ni/MoGe of $\Delta T_c^{\rm trip} = T_c(\alpha = 0^\circ) - T_c(\alpha = 90^\circ) \geqslant 0.7$ K, where α is the angle between the cooling field and the direction of the applied magnetic field. $\alpha = 0^\circ$ corresponds to the P and $\alpha = 90^\circ$ to the perpendicular (PP) orientation of magnetizations of the F1 and F2 layers. Singh *et al.* argued that the giant magnitude of $\Delta T_c^{\rm trip}$ is essentially due to the half-metallic CrO_2 layer. For the further development of SSVs, it is therefore important to verify if this conclusion generally holds for other half-metallic compounds as ferromagnetic parts of an SSV.

With this motivation, we have chosen as a test material the Heusler alloy $Co_2Cr_{1-x}Fe_xAl_y$, named hereafter HA. In our previous work [40], we found that the HA films deposited on the substrate kept at a temperature $T_{\rm sub} \sim 300$ K appear to be a weak ferromagnet, named hereafter HA^{RT}. In contrast, the HA film became practically half-metallic (HA^{hot}) if prepared at $T_{\rm sub} \geqslant 600$ K. Specifically, the degree of the spin polarization (DSP) of its conduction band reaches $70 - 80\%$ [40]. Here, the superscripts RT and hot refer to the room and high temperature values of $T_{\rm sub}$. In the present paper, using HA^{RT} as a weak ferromagnet on the place of the F2 layer in the F1/F2/S structure and HA^{hot} as a "half-metal" on the place of F1 layer, we performed a detailed analysis of the SSV effect in both types of heterostructures, including the appropriate theoretical description of the observed phenomena. Some preliminary data on the use of HA^{RT} and HA^{hot} in different parts of the SSV were reported by us previously in Refs. [41,42].

The paper is organized as follows. The choice of the design and the preparation technique of the SSVs is described in Sec. II. In Sec. III, we describe their magnetic and transport properties. Section IV contains the main experimental data on the SC and SSV properties of the samples. In Sec. V, we introduce the theoretical approach which is used in Sec. VI for the analysis of the obtained results. Finally, the paper is summarized in Sec. VII. Details of the theoretical calculation of the critical temperature T_c of the SSV trilayers are presented in the Appendix.

II. SAMPLES

A. Design of the heterostructures

In previously studied F1/F2/S heterostructures with conventional ferromagnets, we conveniently used the antiferromagnetic CoO_x layer as a bias for the F1 layer (see, e.g., Refs. [11,13,14,36,41]). However, this approach does not work anymore if HA^{hot} is to be used as the F1 layer. At the required deposition of HA^{hot} substrate temperature of $T_{\rm sub} =$ 700 K, CoO_x decomposes, forming ferromagnetic Co, which does not pin the magnetization of HA^{hot}. In this situation, the use of the natural bias of a hard ferromagnet appears to be beneficial. Therefore, in this structure type, the role of the F2 layer adjacent to the SC Pb layer is played by Ni deposited at a low temperature of the substrate $T_{\rm sub} \sim 150$ K. The role of the soft ferromagnet is played by HA^{hot}, which was already deposited before on the substrate held at $T_{\rm sub} \sim 700$ K. Hence, now the magnetization of the F2 layer is not rotated by the operating magnetic field, but that of the F1 layer, while the F2 magnetization remains almost fixed by "self-bias."

The final design of two studied structure types is depicted in Fig. 2.

In structure type 1, the antiferromagnetic cobalt oxide layer is used to fix the direction of the magnetization of the Py layer (F1 layer). This allows rotation of the magnetization direction of the weak ferromagnetic HA^{RT} layer (F2 layer) by changing the direction of the applied external magnetic field. In turn, in structure type 2, the role of the "free rotating" layer is played by the HA^{hot} layer (F1 layer) and the magnetization of the Ni layer (F2 layer) is almost fixed due to a large coercive field. The Ta layer is the seed layer for the growth of the HA^{hot}. The

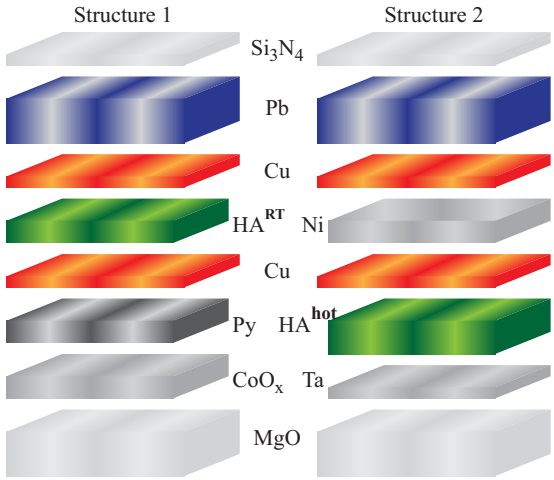

FIG. 2. Two structure types of the SSV studied in the present work (see the text for details).

Cu layer separating the F1 and S layers prevents interdiffusion during the growth of the SSV [43]. The Cu layer between the F1 and F2 layers is used to decouple their magnetizations. Si_3N_4 is the cap protective layer.

B. Preparation

Metallic layers were grown on the high-quality single crystalline MgO(001) substrates using classical e-gun in ultrahigh vacuum (UHV) conditions of about 1×10^{-8} mbar within a closed vacuum cycle. The evaporation chamber has a load-lock station, allowing us to avoid vacuum breaking before the substrate load. The thickness of the layers during the growth was controlled by a standard quartz-crystal monitor. All materials used for evaporation had a purity of better than 4N, i.e., the contamination level could be kept below 0.01 at. %. The substrates were fixed at a small rotating wheel on the sample holder. After that, the sample holder was placed inside the load-lock station. The rotating wheel system allows us to prepare a set of samples with varied thickness at the same evacuation cycle. The cobalt oxide layer in the structures of type 1 was prepared in two stages. First, the Co layer was deposited on the substrate. At the second stage, it was transferred to the load-lock station where the Co layer was oxidized using 2 hours' exposure at 100 mbar of pure oxygen gas. After the oxidation procedure, the samples were returned to the UHV deposition chamber where the process of deposition was continued. At the final stage, the samples were transferred to the neighboring sputtering chamber where they were capped by a 85-nm-thick Si_3N_4 isolating protection layer to prevent the oxidation of the top Pb layer. To prepare high-quality samples, the deposition rate of Pb amounted 1.0–1.2 nm/s, which is very important because at lower deposition rates the transport properties of the Pb layer do not yield the necessary values of the SC coherence length. For other materials, we used the following deposition rates: 0.037 nm/s for HA and 0.05 nm/s for the Cu, Ni, Ta, and Py layers. To optimize the growth of the top fragment containing the Pb layer after the deposition of the HA we decrease T_{sub} down to 150 K and continued the preparation process as in Ref. [44]. The low T_{sub} improves the smoothness of the Pb-layer surface, thus increasing the magnitude of the SSV effect. The parameters of the studied samples are presented in Table I.

TABLE I. Overview of the studied samples of two types of the SSV structures (Fig. 2). Type 1: CoO_x (3.5 nm)/Py (5 nm)/Cu (4 nm)/HA^{RT}(d_{HA})/Cu (1.5 nm)/Pb (80 nm); Type 2: HA^{hot} (20 nm)/Cu (4 nm)/Ni(d_{Ni})/Cu (1.5 nm)/Pb (105 nm).

Structure type	Sample name	d_{HA} (nm)	d_{Ni} (nm)
1	PL3481	0.6	—
	PL3418	1	—
	PL3416	4	—
2	PLAK4212	—	0.9
	PLAK4214	—	1.6
	PLAK4215	—	2.0
	PLAK4216	—	2.5

We emphasize again that the most important difference between the two structure types is the growth temperature of $HA = Co_2Cr_{1-x}Fe_xAl_y$. According to our previous work [40], with $T_{sub} = 300$ K, one obtains a weak ferromagnet HA^{RT} and with $T_{sub} \geqslant 600$ K an almost half-metallic HA^{hot} layer with the spin polarization of the conduction band of 70–80% can be grown.

Finally, we mention that, as we found out before [40], the real stoichiometry of HA^{RT} is actually $Co_2Cr_{0.43}Fe_{0.36}Al_{0.5}$ and that of HA^{hot} is $Co_2Cr_{0.55}Fe_{0.72}Al_{0.62}$. Obviously, there is a deficiency of aluminum in comparison with the ideal Heusler composition $Co_2Cr_{1-x}Fe_xAl$. At the same time, in fact, this "nonideal" composition demonstrates a high DSP of the order of 70%. Husain *et al.* [45] have shown that the DSP increases with increasing the substrate temperature T_{sub}. Therefore we expect its value in our samples to be of the order of 80%.

III. MAGNETIC AND TRANSPORT CHARACTERIZATION

A. Magnetic measurements

All samples were magnetically characterized using a standard 7T VSM SQUID magnetometer, as reported in our preliminary work [41]. The samples of the structure type 1 were cooled down in a magnetic field of 4 kOe applied in the sample plane and measured at $T = 10$ K. Bearing in mind that the Néel temperature of the cobalt oxide is of the order of 250–290 K, after such cooling procedure the magnetization of the Py layer is pinned by the anisotropy field of the antiferromagnetic layer. For the representative sample of type 1 (PL3481) (see Fig. 1 of our work [41]) the magnetization of the free HA^{RT} layer starts to decrease by decreasing the field from +4 kOe to the field of the order of 0.1 kOe. At the same time, the magnetization of the Py layer is kept by the bias CoO_x layer until the magnetic field of −2 kOe is reached. Thus, in the field range between 0.1 and −2 kOe, the mutual orientation of the two layers is AP. While further changing the field from −2 to −2.5 kOe, the magnetization of the Py layer rotates away from the direction of the cooling magnetic field in the direction of the applied field. Qualitatively, this kind of the magnetic hysteresis loop is typical for all samples

of structure type 1. The minor hysteresis loop which arises due to reversal of the magnetization of the F2 layer (HA^{RT}) has been measured in the SSV samples by sweeping the magnetic field H from +1 kOe down to −1 kOe and back to +1 kOe. A typical minor loop for type 1 samples is shown in Fig. 1(b) in Ref. [41]. The measurements were performed for the samples with $d_{HA^{RT}}$ ranging from 0.6 to 7 nm. It was found that the saturation field of the HA decreases gradually (as approximately $1/d_{HA^{RT}}$) from 1 kOe for the sample with $d_{HA^{RT}} = 0.6$ nm down to 0.1 kOe for the sample with $d_{HA^{RT}} = 7$ nm. We found a sharp decrease of the coercive field from 1 kOe for the sample with $d_{HA^{RT}} = 0.6$ nm down to 0.05 kOe for the sample with $d_{HA^{RT}} = 7$ nm. The height of the $M(H)$ loop due to the reversal of the magnetization of the F1 and F2 layers is proportional to the thickness of the respective layers. For example, the change of the magnetization in the major loop in Fig. 1(a) in Ref. [41] due to flip of the magnetization of the pinned F1 layer is approximately five times larger compared to the height of the minor loop in Fig. 1(b) in Ref. [41], in agreement with the ratio of the thicknesses of the respective layers in this representative sample.

As for the samples of structure type 2, one observes the onset of the saturation of the HA^{hot} magnetization at 30 Oe. The magnetic response from the Ni layer is not seen due to a relatively small value of the magnetic moment of this layer. It should be noted that such conventional measurements of the magnetic hysteresis loop for the sample without HA^{hot} by decreasing the magnetic field down to zero and increasing it again in the negative direction are different from the situation when the field vector rotates in the plane of the sample. In the latter case, the magnetization starts to follow the field with a considerable delay.

B. Transport properties

The electrical resistivity was measured using a DC current mode in a standard four-terminal configuration. The temperature of the sample was controlled with the 230-ohm Allen-Bradley resistor thermometer which is particularly sensitive in the temperature range of interest. The current and voltage leads were attached to the sample by clamping contacts. The critical temperature T_c was defined as the midpoint of the transition curve. We found that the residual resistivity ratio $RRR = \rho(300\ K)/\rho(10\ K)$ of the studied samples lies in the interval $10 < RRR < 17$. Using $\rho(300\ K) = 21\ \mu\Omega\,cm$ [46], we obtain $\rho_0 = 1.2$–$2.1\ \mu\Omega\,cm$ for the residual resistivity. The BCS coherence length for Pb amounts to $\xi_0 = 83$ nm [46] and the mean-free path of the conduction electrons obtained using the Pippard relations [47] is about $l_S = 17$ nm. The comparison of l_S with ξ_0 shows that $l_S \ll \xi_0$, implying the "dirty" limit for the SC part of the system.

Thus, the residual resistivity at 4 K $\rho(4K)$ was found to be equal to 1.5 $\mu\Omega\,cm$. The corresponding SC coherence length reads

$$\xi_S = \sqrt{\frac{\hbar D_S}{2\pi k_B T_{cS}}}. \quad (1)$$

Here $T_{cS} = 7.18$ K is the critical temperature of the SC Pb layer; D_S is the diffusion constant in the SC layer. For all studied samples we obtain using Eq. (1), $\xi_S = 41$ nm.

We also tried to estimate the residual resistivity of the F2 layer in both structure types in the thickness range corresponding to the studied SSV samples. We cannot measure directly the partial resistivity of each layer. The main contribution to the residual resistivity of the F2 layers is given by the surface relaxation of conduction electrons and, therefore, by the roughness of the F layers. Hence, we measured resistivity of such thin layers using a single layer or bilayer films. It turns out that the HA^{RT} and Ni films grown directly on the MgO substrate at room temperature become discontinuous at thicknesses below 10 nm. Therefore, we prepared a set of samples MgO/Cu(4 nm)/HA($d_{HA^{RT}}$) and MgO/Cu(4 nm)/Ni(d_{Ni}). For them, the quality of the HA^{RT} and Ni layers was much better, and we obtained $\rho_0^{Ni} \sim 40 - 50\ \mu\Omega\,cm$. Such a big scatter of the resistivity values is caused by different roughnesses of the layers. Possibly, the residual resistivity of the Ni layers in the respective SSV could be different. In our analysis below, we shall use an "optimistic" value of the residual resistivity for the Ni layer $\rho_0^{Ni} = 40\ \mu\Omega\,cm$. Similar to our previous work [43], we obtain $D_F^{Ni} = 2.5\ cm^2/s$.

The nonmagnetic coherence length in the F layers is defined as $\xi_F = \sqrt{\hbar D_F/2\pi k_B T_{cS}}$. From this equation, we get $\xi_F^{Ni} = 6.3$ nm. As for the HA layers, the coherence length obtained from the resistivity differs considerably from that obtained from the fitting of the theory to the experimental data. For the films prepared at $T_{sub} = 300$ K, we obtain that the resistivity does not depend on temperature and amounts to $\rho_F \simeq 143\ \mu\Omega\,cm$ (cf. 220 $\mu\Omega\,cm$ in Ref. [48] and 170 $\mu\Omega\,cm$ in Ref. [49]). For the film prepared at $T_{sub} = 700$ K, we obtain $\rho_F \simeq 130\ \mu\Omega\,cm$ (cf. 330 $\mu\Omega\,cm$ in Ref. [48] and 170 $\mu\Omega\,cm$ in Ref. [49]).

C. Dependence of the superconducting transition temperature on the Pb-layer thickness

It is important to find the optimal Pb-layer thickness for the observation of the F/S proximity effect. In general, the Pb layer should be sufficiently thin to make the whole SC layer sensitive to the magnetic part of the structure. The optimal thicknesses of the Pb layer for both structure types were determined from the $T_c(d_{Pb})$ curves for the HA^{RT}/Cu/Pb and Ni/Cu/Pb trilayers measured at constant $d_{HA^{RT}} = 12$ nm and $d_{Ni} = 5$ nm, respectively (for preliminary data see our work [42]).

At large Pb-layer thicknesses, T_c slowly decreases with decreasing d_{Pb}. Below $d_{Pb} \sim 60$ nm for HA^{RT}/Cu/*Pb* T_c and $d_{Pb} \sim 130$ nm for Ni/Cu/Pb the T_c value starts to decrease rapidly. Below $d_{Pb} \sim 30$ nm and below $d_{Pb} \sim 80$ nm, in the corresponding cases, T_c is less than 1.5 K. At small thicknesses, the width of the SC transition curves δT_c gets extremely large, of the order of 0.4 K. Bearing in mind that the influence of the magnetic part is stronger at small Pb-layer thicknesses, we have chosen $d_{Pb} = 80$ and 105 nm as the optimal thicknesses for the SSV structures containing HA^{RT} and Ni-based F2 layers, respectively.

Moreover, the above experiment is the standard procedure for a simple estimation of the boundary parameters. For that, one measures the T_c (d_{Pb}) dependence at fixed ferromagnetic layer thickness larger than the penetration depth of the Cooper pairs in the ferromagnetic layers ξ_h. We estimated it for Ni

as 5 nm and obtained the critical thickness of the SC layer $d_s^{\rm crit} \sim 79$ nm, below which superconductivity vanishes. For structures type 1, we obtained $d_s^{\rm crit} \sim 23$ nm.

Further, following Ref. [50], we found the Kurpiyanov-Lukichev boundary resistance parameter [51] $\gamma_{b\rm FS}$ for the F/S interface [the exact definition is given below, in Eqs. (3)]. It was approximated by $\gamma_{b\rm FS} = 0.37$ for structure type 1 and by $\gamma_{b\rm FS} = 0.1$–0.4 for structure type 2.

IV. EXPERIMENTAL RESULTS

A. Structure type 1

To study the angular dependence of T_c on the mutual orientation of the magnetizations, we used essentially the same protocol as for the preparation of the magnetizations of F1 and F2 layers, which was used for the measurement of the minor hysteresis loop: the P and AP mutual orientations of the magnetizations of the two layers were achieved at fields $H_0 = +1$ and -1 kOe, respectively. For these fields, both magnetizations of the F layers are P or AP aligned for all thicknesses of the studied HA$^{\rm RT}$ layers.

Typically, for the samples of type 1, the maximum magnitude of $\Delta T_c^{\rm full}$ is achieved when the mutual orientation of the magnetizations is changed from the collinear to the orthogonal one and amounts to ~0.05 K (see Figs. 2(c) and 3(c) in Ref. [41]). For a set of the SSV samples with different $d_{\rm HA^{RT}}$, we measured the dependence of the T_c value on the angle α between the direction of the cooling field and the external magnetic field, both applied in the sample plane.

As can be seen from Fig. 3, while changing the mutual orientation of the magnetizations by the gradual in-plane rotation of the magnetic field from P ($\alpha = 0^\circ$) to the AP ($\alpha = 180^\circ$) state, T_c does not change monotonically but passes through a minimum. According to theory [12], the characteristic minimum of the $T_c(\alpha)$ dependence is a fingerprint of LRTC.

Although the triplet component is inherent in the case of the noncollinear magnetizations, assuming for a moment its absence one would expect a monotonic $T_c(\alpha)$ dependence [52]. From the symmetry arguments, $T_c(\alpha)$ should behave as α^2 and $(\pi - \alpha)^2$ when α deviates from 0 and π, respectively (since deviations in both limits of these values are physically equivalent and we expect $T_c(\alpha)$ to be an analytical function). Then one comes to a simple angular superposition of the limiting values T_c^P and $T_c^{\rm AP}$, which reads $T_c^{\rm ref}(\alpha) = T_c^P \cos^2(\alpha/2) + T_c^{\rm AP} \sin^2(\alpha/2)$. This dependence is shown by the dashed lines in Figs. 3 and 6, and we treat them as reference curves. Deviation of the actual T_c from the reference curve then shows the contribution of LRTC to ΔT_c.

From Fig. 3(a), where the angular dependence of T_c for the sample PL3416 is presented, we obtain the value of the singlet SSV effect $\Delta T_c = -25$ mK. The negative sign implies that we observe the inverse SSV effect due to the destructive interference of the Cooper pairs wave function in the heterostructure [13].

From Fig. 3(b), we extract the magnitude of $\Delta T_c \sim 85$ mK for the sample PL3418 with the positive sign corresponding to the direct SSV effect. As can be seen from Fig. 3(b), the difference $T_c^{\rm P} - T_c^{\rm PP}$ amounts up to 100 mK. Therefore, the magnitude of the SSV effect with the change of the mutual orientation of the magnetizations from AP to PP exceeds the width of the SC transition curve $\delta T_c = 70$ mK. Therefore, there is a possibility of switching on/off the SC current fully. As seen from Fig. 2(c) in Ref. [41], the full switching $\Delta T_c^{\rm full} \sim 50$ mK is still not very large but, nevertheless, it is five times larger than in the first observation of the full SSV effect in Ref. [11].

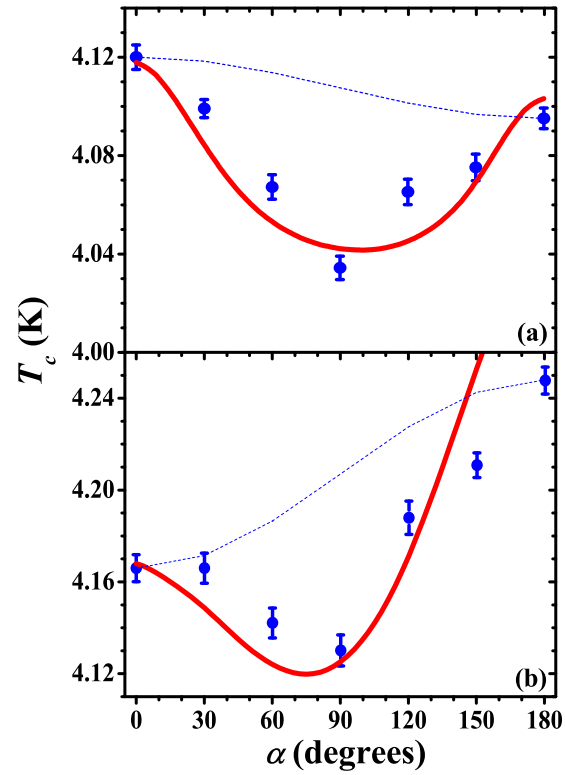

FIG. 3. Dependence of T_c on the angle α between the direction of the cooling field used to fix the direction of the magnetization of the Py layer and the applied magnetic field $H_0 = +1$ kOe that rotates the magnetization of the HA$^{\rm RT}$ layer for samples PL3416 (a) and PL3418 (b) (experimental data points are reproduced from Ref. [41]). Dashed lines depict the estimated angular dependence of the singlet SSV effect. Solid lines are the theoretical curves with the parameters obtained in Sec. VI (see the text for details).

B. Structure type 2

Considering the results of the measurements of the $M(H)$ hysteresis loop of the SSV samples with structure type 2, we assumed initially that to manipulate the magnetization direction of the HA layer, the magnetic field of the order of 30 Oe should be enough. We performed such experiments and find a disappointingly small SSV effect. Surprisingly, we found that with increasing the magnetic field the triplet contribution to the SSV effect linearly increases with magnetic field. For example, for the sample PLAK4216 $\Delta T_c^{\rm trip}$ increases linearly up to 0.4 K at 2 kOe (Fig. 4). Notably, a similar increase of $\Delta T_c^{\rm trip}$ was observed by Singh *et al.* [39] as well, and, similar to us, they did not find conclusive explanation for this surprising observation. Obviously, this field-dependent effect observed by two groups on different samples is a very

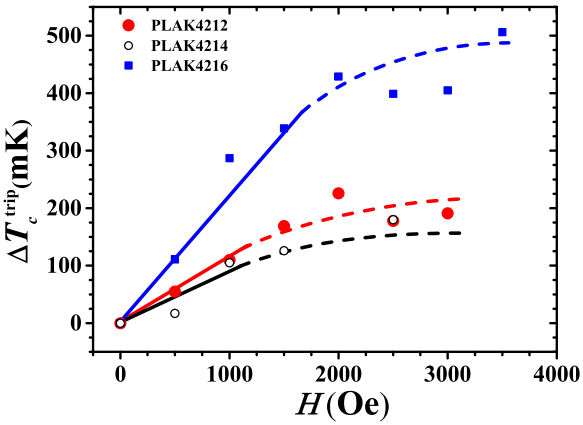

FIG. 4. The magnitude of the triplet SSV effect $\Delta T_c^{\rm trip}$ as a function of the applied magnetic field. Lines are guides for the eye. Experimental data points for sample PLAK4216 are reproduced from Ref. [42].

important finding as it appears to be a salient feature of the new type of SSVs and needs theoretical explanation.

Figure 5 shows the SC transition curves for sample PLAK4216 measured in a strong magnetic field. The shift of the curves between the P and PP orientations $\Delta T_c^{\rm trip}$ amounts to 0.51 K. Other samples demonstrate a smaller effect (cf. Fig. 4). Figure 6 depicts the dependence of T_c on α for two different samples. It appears qualitatively similar to the ones observed previously in Refs. [14,36,41], reaching a minimum near $\alpha = 90^\circ$. However, the minimum which we observe now is much deeper, suggesting that the SSV effect is dominated by the spin polarized (triplet) Cooper pairs. Indeed, the estimated contribution of the singlet SSV effect depicted by dashed lines in Fig. 6 is practically negligible.

For the samples with structure type 2 showing a large magnitude of the SSV effect, we observe an increase of δT_c at the PP configuration of the magnetizations (Fig. 5). In addition, the magnitude of the triplet SSV effect $\Delta T_c^{\rm trip}$ depends on the applied magnetic field up to a certain value of H_0 which is different for different samples (Fig. 4).

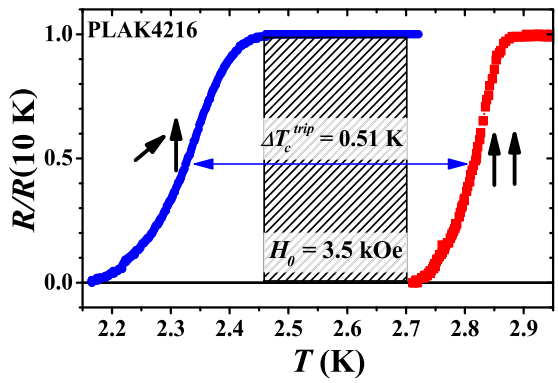

FIG. 5. Record splitting of the SC transition curves for the P and PP configurations of the magnetization of the Ni layer and the applied magnetic field $H_0 = 3.5$ kOe which rotates the magnetization of the $HA^{\rm hot}$ layer for the sample PLAK4216 (experimental $R(T)$ dependencies are reproduced from Ref. [42]). Shaded rectangle marks the operational area of the SSV.

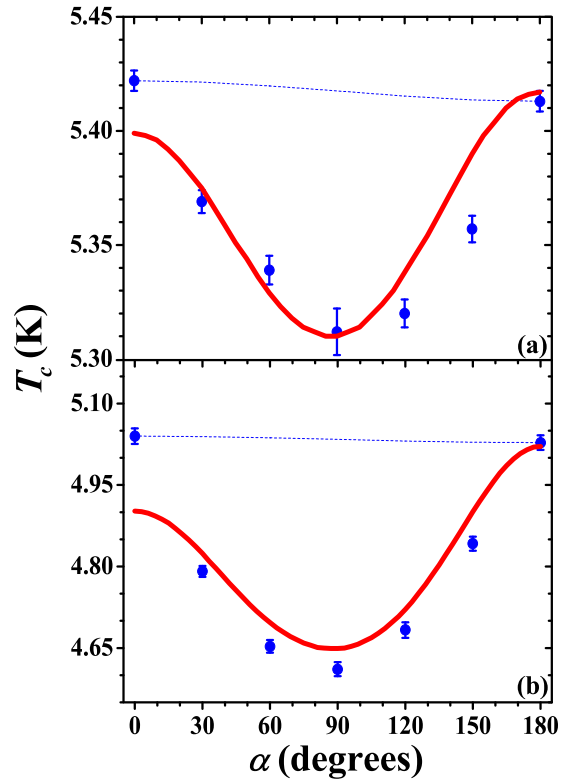

FIG. 6. Dependence of T_c on the angle α between the direction of the cooling field used to fix the direction of the magnetization of the Ni layer and the applied magnetic field $H_0 = 1$ kOe which rotates the magnetization of the $HA^{\rm RT}$ layer for samples PLAK4212 (a) and for the sample PLAK4216 (b) (experimental points in (b) are reproduced from Ref. [42]). Dashed lines depict the estimated angular dependence of the singlet SSV effect. Solid lines are the theoretical curves with the parameters obtained in Sec. VI (see the text for details).

V. THEORY

The theoretical approach that we employ for the analysis of experiment in Figs. 3 and 6 is based on the Usadel-equation technique [53] and generalizes the method of Ref. [12] along the lines of Ref. [54]. It allows us to consider layered structures with different material parameters of all the layers and arbitrary Kupriyanov-Lukichev (KL) boundary parameters [51] of all the interfaces.

Each of the two interfaces (F1/F2 and F2/S) is described by the matching parameter γ and the resistance parameter γ_b. Introducing the (nonmagnetic) coherence lengths of the F layers as

$$\xi_{F1} = \sqrt{\frac{\hbar D_{\rm F1}}{2\pi k_B T_{\rm cS}}}, \quad \xi_{F2} = \sqrt{\frac{\hbar D_{\rm F2}}{2\pi k_B T_{\rm cS}}}, \tag{2}$$

where $T_{\rm cS}$ is the bulk critical temperature of the superconductor (or, equivalently, the critical temperature of an isolated S

TABLE II. Parameters used for fitting the experimental data on $T_c(\alpha)$ for the CoO_x (3.5 nm)/Py (5 nm)/Cu (4 nm)/HA($d_{HA^{RT}}$)/Cu (1.5 nm)/Pb (80 nm) SSV of structure type 1.

	PL3418	PL3416
d_{HA}, nm	1	4
ξ_S, nm	41	41
ξ_{F2}, nm	14	14
ξ_{F1}, nm	7.5	7.5
γ_{FS}	0.185	0.199
γ_{bFS}	0.37	0.37
γ_{FF}	1	1
γ_{bFF}	0	0
h_2, eV	0.1	0.1
h_1, eV	1	1

layer), we can define the KL interface parameters as [54]

$$\gamma_{FF} = \frac{\rho_{F2}\xi_{F2}}{\rho_{F1}\xi_{F1}}, \quad \gamma_{bFF} = \frac{R_{bFF}\mathcal{A}}{\rho_{F1}\xi_{F1}},$$
$$\gamma_{FS} = \frac{\rho_S\xi_S}{\rho_{F2}\xi_{F2}}, \quad \gamma_{bFS} = \frac{R_{bFS}\mathcal{A}}{\rho_{F2}\xi_{F2}}, \tag{3}$$

where ρ with a subscript is the resistivity of the corresponding layer, $\mathcal{A}$ is the interface area, while R_{bFF} and R_{bFS} are the interface resistances of the F1/F2 and F2/S interfaces, respectively.

The necessity to consider arbitrary F1/F2 interface parameters is due to different materials of the two F layers. This is a new theoretical ingredient, in comparison to fittings of our previous experiments in Refs. [14,43,52].

Details of the theory are presented in the Appendix.

VI. ANALYSIS

Our theory (Sec. V and Appendix) containsnine fitting parameters. Our transport measurements allow us to reduce this number down to four. We took ρ_S and ξ_S and also ρ_0^{Ni} and ξ_F as estimated in Sec. III.B (rows 2 and 3 in Tables II and III) Then using Eqs. (3), we determine γ_{FS} (rows 5 in Tables II and III) and γ_{FF} (row 7 in Tables II and III). As a rough approximation, we use the theoretical results of Ref. [50] for

TABLE III. Parameters used for fitting the experimental data on $T_c(\alpha)$ for the MgO/Ta(5 nm)/\$-HA^{hot} (20 nm)/Cu (4 nm)/Ni(d_{Ni})/Cu (1.5 nm)/Pb (105 nm) SSV of structure type 2.

	PLAK4212	PLAK4214	PLAK4216
d_{Ni}, nm	0.9	1.6	2.5
ξ_S, nm	41	41	41
ξ_{F2}, nm	6.25	6.25	6.25
ξ_{F1}, nm	40	40	40
γ_{FS}	0.165	0.164	0.1
γ_{bFS}	0.4	0.35	0.1
γ_{FF}	1	1	1
γ_{bFF}	1.5	1	0.1
h_2, eV	0.03	0.03	0.03
h_1, eV	0.39	0.39	0.39

d_S^{crit} which can be estimated in the limit $(\gamma/\gamma_b)(d_S/\xi_S) \ll 1$ as

$$\frac{d_S^{crit}}{\xi_S} = 2\gamma_E\left(\frac{\gamma}{\gamma_b}\right). \tag{4}$$

Here $\gamma_E = 1.78$ is the Euler constant. The value of $\gamma_b = 0$ corresponds to the fully transparent F/S interface. d_S^{crit} is smaller for a larger value of γ_b. We use $\rho_S \simeq 1.6\,\mu\Omega\,\text{cm}$, $\xi_S = 41$ nm, and $\rho_F \simeq 130\,\mu\Omega\,\text{cm}$. At the beginning, from Eqs. (3), we obtain $\gamma_{FS} \simeq 0.034$ for both series of the samples. Then, taking into account that $d_{Pb}^{crit} = 23$ nm for the structure type 1 and $d_{Pb}^{crit} = 79$ nm for structure type 2, we find from Eq. (4) the values of $\gamma_{bFS} \simeq 0.2$ and $\simeq 0.65$, respectively. Using these parameters as starting values we have fitted the theoretical curves $T_c(d_{Pb})$. The optimal values of the parameters obtained by the fitting are shown in Tables II and III. Obviously, the theory and experiment agree reasonably well.

Finally, we comment on the $\gamma_{bFF} = 0$ choice for type I samples. We work within the Usadel equations with KL boundary conditions, and the latter contain the interface resistance R as a parameter. These are model boundary conditions, and different band structures on the two sides of the interface are not taken into account within this framework. So, R in the KL boundary conditions originates from a barrier at the interface. Of course, in reality, a difference of the band structures can also contribute to R, but there is no easy way to take this effect into account. As long as we do not expect insulating barrier at the interface, we try fitting with $R = 0$ (hence, $\gamma_{bFF} = 0$). Poor fitting results in this case would tell us that either a barrier exists or that the band-structure mismatch cannot be neglected. At the same time, the result of the fitting in Figs. 3 and 6 looks satisfactory. This signifies that our initial guess of $\gamma_{bFF} = 0$ was reasonable, so we go on with this value.

A. Structure type 1

Up to now, the switching of the SC current was performed by changing the mutual direction of the magnetizations of the F layers from AP to P orientation (see, e.g., Fig. 1) or by combination of the singlet and triplet SSV effect (Fig. 2 in Ref. [36]). In both cases, the full switching between AP and PP configurations of magnetizations was obtained. It should be noted that for the sample PL3416 the difference $T_c^{AP} - T_c^{P} = 60$ mK is smaller than the difference between the P and PP configurations which amounts to 100 mK. Thus, the main role in the switching is played by the triplet contribution.

B. Structure type 2

A remarkably large separation of the SC transition curves for the P and PP orientation of magnetizations of F1 and F2 layers in Fig. 5, yielding the value of ΔT_c^{trip} up to 0.5 K, evidence of the prominent spin-triplet SC correlations in our samples. Figure 6 demonstrates that the theory correctly reproduces characteristic features of the $T_c(\alpha)$ dependence (triplet SSV behavior) with parameters listed in Table III.

Figure 5 shows that ΔT_c^{full} for this sample is of the order of 0.51 K. This value is 30 times larger than was obtained in Ref. [11].

As can be seen in Fig. 4, $\Delta T_c^{\rm trip}$ increases with increasing the strength of the applied magnetic field. At first glance, it is surprising that $\Delta T_c^{\rm trip}$ continues to increase well above the saturation magnetic field for the $HA^{\rm hot}$ layer. We suppose that this may be caused by some magnetic inhomogeneity of the $HA^{\rm hot}$ layer reflected in a slight increase of its magnetization, where more and more "microdomains" become gradually involved in the formation of the total moment just as it was observed by Singh *et al.* [39].

The obtained experimental results show that as a result of the optimal choice of materials for F layers, the triplet contribution is probably always dominant in the SSV effect. According to the results of the present paper and the data of Ref. [39], it appears that, indeed, a half-metallic compound is possibly the best presently known candidate for the material of the F1 layer in the F1/F2/S SSV. Its efficiency is likely related to the fact that electrons incident on the surface of a half metal can only penetrate into it when they have a certain direction of spin. This also concerns the spin-polarized Cooper pairs which, depending on their specific spin orientation, will be either reflected from the S/F interface or easily penetrate through it.

VII. CONCLUSIONS

By studying the SSV multilayers $Co_2Cr_{1-x}Fe_xAl$/Cu/Ni/Pb whose magnetic part contains the Heusler alloy $Co_2Cr_{1-x}Fe_xAl$ with different degree of spin polarization of the conduction band, we have obtained a large SSV effect due to the LRTC of the SC condensate $\Delta T_c^{\rm trip} \sim 0.5$ K at a moderate applied field of 3.5 kOe as compared with the earlier work in Ref. [39].

In particular, finding the most appropriate half metal with a high degree of spin polarization of the conduction band for the F layer in the SSV appears to be a crucial issue. At present, it allows us to increase the area of the full switching $\Delta T_c^{\rm full}$ up to 0.3 K which is 30 times larger than that obtained in the first experiment [11]. Furthermore, noting first theoretical attempts to include the half metal into the SSV construction in Refs. [56,57], our data as well as the results by Singh *et al.* [39] call for a comprehensive quantitative theoretical treatment to obtain further insights into exciting physics of the triplet SSVs.

ACKNOWLEDGMENTS

Ya.V.F. was partially supported by the RAS program Contemporary Problems of Low-Temperature Physics, by the Russian Foundation for Basic Research (RFBR) (Grant No. 19-52-50026), and by the Basic research program of HSE.

APPENDIX: THEORY OF T_C IN FFS TRILAYERS

In this Appendix, we present the theoretical method for calculating and analyzing the critical temperature of diffusive F1/F2/S trilayers (see Fig. 7) in the framework of the Usadel equation [53] and KL boundary conditions [51]. Within this framework, we consider the general situation assuming different exchange fields h_1 and h_2 in the F layers and arbitrary KL parameters γ and γ_b of the two interfaces (F1/F2 and F2/S).

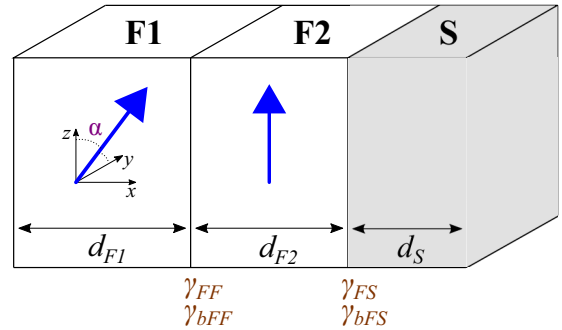

FIG. 7. F1/F2/S trilayer. The F2/S interface corresponds to $x = 0$. The thick blue arrows in the F layers denote the exchange fields lying in the (y, z) plane. The angle between the in-plane exchange fields h_1 and h_2 is α. Each of the two interfaces (denoted as FF and FS) is characterized by two interface parameters, γ and γ_b, see Eqs. (3).

This full proximity-effect model, generalizing the model of Ref. [12], has been previously analyzed in Refs. [54] (see also Ref. [55]); however, the theoretical formalism was only briefly outlined. Here, we present details of the corresponding derivation. In particular, we formulate explicit matrix equation for determining the interface function W. This function directly determines suppression of T_c in the structure.

As shown in Fig. 7, the S layer is of thickness d_S ($0 < x < d_S$), the middle F layer is of thickness d_{F2} ($-d_{F2} < x < 0$), the outer F layer is of thickness d_{F1} ($-d_{F1} - d_{F2} < x < -d_{F2}$), the x axis is normal to the plane of the layers. The exchange field in the middle F layer is along the z direction, $h_2 = (0, 0, h_2)$, while the exchange field in the outer F layer is in the yz plane: $h_1 = (0, h_1 \sin\alpha, h_1 \cos\alpha)$.

Near T_c, the Usadel equations are linearized and contain only the anomalous Green function $\check{f}$ [20,58]:

$$\frac{\hbar D}{2}\frac{d^2\check{f}}{dx^2} - |\omega|\check{f} - \frac{i\,\mathrm{sgn}\,\omega}{2}\{\hat{\tau}_0(\mathbf{h}\hat{\boldsymbol{\sigma}}), \check{f}\} + \Delta\hat{\tau}_1\hat{\sigma}_0 = 0. \quad \text{(A1)}$$

Here, $\check{f}$ is a 4×4 matrix, $\hat{\tau}_i$ and $\hat{\sigma}_i$ are the Pauli matrices in the Nambu-Gor'kov and spin spaces, respectively, D is the diffusion constant, and $\omega = \pi k_B T_c(2n + 1)$ with integer n is the Matsubara energy. The order parameter Δ is real-valued in the S layer, while in the F layers it is zero. The diffusion constant D acquires a proper subscript (F1, F2, or S) when Eq. (A1) is applied to the corresponding layer.

The KL boundary conditions [51] for the anomalous Green functions in the three layers can be written in term of the KL interface parameters Eqs. (3) as follows. At the F1/F2 interface ($x = -d_{F2}$),

$$\check{f}_{F2} = \check{f}_{F1} + \gamma_{bFF}\xi_{F1}\frac{d\check{f}_{F1}}{dx}, \quad \text{(A2)}$$

$$\xi_{F2}\frac{d\check{f}_{F2}}{dx} = \gamma_{FF}\xi_{F1}\frac{d\check{f}_{F1}}{dx}. \quad \text{(A3)}$$

At the F2/S interface ($x = 0$),

$$\check{f}_S = \check{f}_{F2} + \gamma_{bFS}\xi_{F2}\frac{d\check{f}_{F2}}{dx}, \quad \text{(A4)}$$

$$\xi_S\frac{d\check{f}_S}{dx} = \gamma_{FS}\xi_{F2}\frac{d\check{f}_{F2}}{dx}. \quad \text{(A5)}$$

At the outer surfaces of the structure (i.e., at $x = -d_{F1} - d_{F2}$ and $x = d_S$), $d\check{f}/dx = 0$.

The anomalous Green's function $\check{f}$ can be expanded into the following components:

$$\check{f} = \hat{\tau}_1(f_0\hat{\sigma}_0 + f_3\hat{\sigma}_3 + f_2\hat{\sigma}_2), \tag{A6}$$

where f_0 is the singlet component, f_3 is the triplet with zero projection on the z axis, and f_2 is the triplet with ± 1 projections on z (the latter is present only if $\alpha \neq 0, \pi$). The singlet component is even in ω (and real valued), while the triplet ones are odd (and imaginary): $f_0(-\omega) = f_0(\omega)$, $f_3(-\omega) = -f_3(\omega)$, and $f_2(-\omega) = -f_2(\omega)$, which makes it sufficient to consider only positive Matsubara energies, $\omega > 0$.

The problem of calculating T_c in the FFS structure can be reduced [12,54] to an effective set of equations for the singlet component in the S layer: the set includes the self-consistency equation and the Usadel equation,

$$\Delta \ln\frac{T_{cS}}{T_c} = 2\pi T_c \sum_{\omega>0}\left(\frac{\Delta}{\omega} - f_0\right), \tag{A7}$$

$$\frac{\hbar D_S}{2}\frac{d^2 f_0}{dx^2} - \omega f_0 + \Delta = 0, \tag{A8}$$

with the boundary conditions

$$\xi_S \frac{df_0}{dx} = W f_0\Big|_{x=0}, \quad \frac{df_0}{dx} = 0\Big|_{x=d_S}. \tag{A9}$$

This is exactly the problem for which the multimode solution procedure (as well as the fundamental-solution method) was developed in Refs. [50,59].

The difference of our current consideration from previous analysis of FFS structures [12] is the generalized form of W in Eqs. (A9). This interface function contains information about the part of the structure attached to the S layer (including, in particular, information about the magnitudes and orientations of the exchange fields and properties of the interfaces). In addition to exact calculation of T_c, knowledge of the (real) interface function W can be used for qualitative analysis of T_c behavior as a function of system's parameters since larger W implies stronger suppression of T_c. So, our goal is to calculate W.

The Usadel Eq. (A1) generates the following characteristic wave vectors (the exchange fields h_1 and h_2 are in energy units):

$$k_\omega = \sqrt{\frac{2\omega}{\hbar D_S}}, \quad k_{\omega 1} = \sqrt{\frac{2\omega}{\hbar D_{F1}}}, \quad k_{\omega 2} = \sqrt{\frac{2\omega}{\hbar D_{F2}}},$$

$$k_{h1} = \sqrt{\frac{h_1}{\hbar D_{F1}}}, \quad q_{h1} = \sqrt{k_{\omega 1}^2 + 2ik_{h1}^2},$$

$$k_{h2} = \sqrt{\frac{h_2}{\hbar D_{F2}}}, \quad q_{h2} = \sqrt{k_{\omega 2}^2 + 2ik_{h2}^2}. \tag{A10}$$

Only k_ω appears in the solution for the S layer, while the F-layer solutions are described by $k_{\omega j}$, q_{hj}, and q_{hj}^* (where $j = 1, 2$ is the number of the F layer). Since the exchange energy is usually larger than the SC energy scale, $h_j \gg T_c$, the $k_{\omega j}$ modes in the F layers (arising at noncollinear magnetizations) represent the LRTC [20], which plays the key role in the present paper.

In the S layer, the solution of Eq. (A1) is

$$\begin{pmatrix} f_0(x) \\ f_3(x) \\ f_2(x) \end{pmatrix} = \begin{pmatrix} f_0(x) \\ 0 \\ 0 \end{pmatrix} + \begin{pmatrix} 0 \\ A \\ B \end{pmatrix} \frac{\cosh\left(k_\omega(x - d_S)\right)}{\cosh(k_\omega d_S)}, \tag{A11}$$

where A and B are purely imaginary. The singlet component $f_0(x)$ in the S layer cannot be written explicitly, since it is self-consistently related to the (unknown) order parameter $\Delta(x)$ by Eqs. (A7)–(A8). Our strategy now is to obtain the effective boundary conditions Eqs. (A9) for $f_0(x)$, eliminating all other components in the three layers.

In the middle F2 layer,

$$\begin{aligned}\begin{pmatrix} f_0(x) \\ f_3(x) \\ f_2(x) \end{pmatrix} =& C_1 \begin{pmatrix} 0 \\ 0 \\ 1 \end{pmatrix} \cosh(k_{\omega 2}x) + S_1 \begin{pmatrix} 0 \\ 0 \\ 1 \end{pmatrix} \sinh(k_{\omega 2}x) \\ &+ C_2 \begin{pmatrix} 1 \\ 1 \\ 0 \end{pmatrix} \cosh(q_{h2}x) + C_3 \begin{pmatrix} -1 \\ 1 \\ 0 \end{pmatrix} \cosh(q_{h2}^* x) \\ &+ S_2 \begin{pmatrix} 1 \\ 1 \\ 0 \end{pmatrix} \sinh(q_{h2}x) + S_3 \begin{pmatrix} -1 \\ 1 \\ 0 \end{pmatrix} \sinh(q_{h2}^* x),\end{aligned} \tag{A12}$$

where C_1 and S_1 are purely imaginary, while $C_3 = -C_2^*$ and $S_3 = -S_2^*$.

Finally, in the outer F1 layer,

$$\begin{aligned}\begin{pmatrix} f_0(x) \\ f_3(x) \\ f_2(x) \end{pmatrix} =& E_1 \begin{pmatrix} 0 \\ -\sin\alpha \\ \cos\alpha \end{pmatrix} \frac{\cosh\left(k_{\omega 1}(x + d_{F1} + d_{F2})\right)}{\cosh(k_{\omega 1} d_{F1})} \\ &+ E_2 \begin{pmatrix} 1 \\ \cos\alpha \\ \sin\alpha \end{pmatrix} \frac{\cosh\left(q_{h1}(x + d_{F1} + d_{F2})\right)}{\cosh(q_{h1} d_{F1})} \\ &+ E_3 \begin{pmatrix} -1 \\ \cos\alpha \\ \sin\alpha \end{pmatrix} \frac{\cosh\left(q_{h1}^*(x + d_{F1} + d_{F2})\right)}{\cosh(q_{h1}^* d_{F1})},\end{aligned} \tag{A13}$$

where E_1 is purely imaginary and $E_3 = -E_2^*$.

Altogether, Eqs. (A2)-(A5) produce 12 scalar boundary conditions at the two interfaces (F1/F2 and F2/S). We are mainly interested in one of them, determining the derivative of the singlet component on the S side of the F2/S interface ($x = 0$):

$$\xi_S \frac{df_0}{dx}\Big|_{x=0} = 2\gamma_{FS}\xi_{F2}\,\mathrm{Re}\,(q_{h2}S_2). \tag{A14}$$

The remaining 11 boundary conditions form a system of 11 linear equations for 11 coefficients entering

Eqs. (A11)–(A13):

$$\hat{M}\begin{pmatrix} C_1 \\ C_2 \\ C_3 \\ S_1 \\ S_2 \\ S_3 \\ E_1 \\ E_2 \\ E_3 \\ A \\ B \end{pmatrix} = \begin{pmatrix} f_0(0) \\ 0 \\ 0 \\ 0 \\ 0 \\ 0 \\ 0 \\ 0 \\ 0 \\ 0 \\ 0 \end{pmatrix}. \tag{A15}$$

The solution of this system is nonzero due to $f_0(0)$ in the right-hand side of the system. Finding the S_2 coefficient [which is proportional to $f_0(0)$], we substitute it into Eq. (A14) and thus explicitly find W entering the effective boundary conditions Eqs. (A9).

The $\hat{M}$ matrix (size 11×11) contains only 53 nonzero elements, which are given by the following relations:

$$\begin{aligned}
M_{1,2} &= -M_{1,3} = M_{2,2} = M_{2,3} = M_{3,1} = -M_{2,10} \\
&= -M_{3,11} = 1, \\
M_{1,5} &= M_{2,5} = -M^*_{1,6} = M^*_{2,6} = \gamma_{b\mathrm{FS}} q_{h2} \xi_{\mathrm{F2}}, \\
M_{4,5} &= M^*_{4,6} = -\gamma_{\mathrm{FS}} q_{h2} \xi_{\mathrm{F2}}, \\
M_{3,4} &= \gamma_{b\mathrm{FS}} k_{\omega 2} \xi_{\mathrm{F2}}, \quad M_{5,4} = -\gamma_{\mathrm{S}} k_{\omega 2} \xi_{\mathrm{F2}}, \\
M_{4,10} &= M_{5,11} = -k_\omega \xi_S \tanh(k_\omega d_{\mathrm{S}}), \\
M_{6,2} &= M_{7,2} = -M^*_{6,3} = M^*_{7,3} = \cosh(q_{h2} d_{\mathrm{F2}}), \\
M_{6,5} &= M_{7,5} = -M^*_{6,6} = M^*_{7,6} = -\sinh(q_{h2} d_{\mathrm{F2}}), \\
M_{8,1} &= \cosh(k_{\omega 2} d_{\mathrm{F2}}), \quad M_{8,4} = -\sinh(k_{\omega 2} d_{\mathrm{F2}}), \\
M_{9,2} &= M_{10,2} = -M^*_{9,3} = M^*_{10,3} = q_{h2} \xi_{\mathrm{F2}} \sinh(q_{h2} d_{\mathrm{F2}}), \\
M_{9,5} &= M_{10,5} = -M^*_{9,6} = M^*_{10,6} = -q_{h2} \xi_{\mathrm{F2}} \cosh(q_{h2} d_{\mathrm{F2}}), \\
M_{11,1} &= k_{\omega 2} \xi_{\mathrm{F2}} \sinh(k_{\omega 2} d_{\mathrm{F2}}), \\
M_{11,4} &= -k_{\omega 2} \xi_{\mathrm{F2}} \cosh(k_{\omega 2} d_{\mathrm{F2}}), \\
M_{7,7} &= -M_{8,7} \tan\alpha = [1 + \gamma_{b\mathrm{FF}} k_{\omega 1} \xi_{\mathrm{F1}} \tanh(k_{\omega 1} d_{\mathrm{F1}})] \sin\alpha, \\
M_{10,7} &= -M_{11,7} \tan\alpha = -\gamma_{\mathrm{FF}} k_{\omega 1} \xi_{\mathrm{F1}} \tanh(k_{\omega 1} d_{\mathrm{F1}}) \sin\alpha, \\
M_{6,8} &= -M^*_{6,9} = -[1 + \gamma_{bFF} q_{h1} \xi_{F1} \tanh(q_{h1} d_{F1})], \\
M_{7,8} &= M_{6,8} \cos\alpha, \quad M_{8,8} = M_{6,8} \sin\alpha, \\
M_{7,9} &= -M_{6,9} \cos\alpha, \quad M_{8,9} = -M_{6,9} \sin\alpha, \\
M_{9,8} &= -M^*_{9,9} = \gamma_{\mathrm{FF}} q_{h1} \xi_{\mathrm{F1}} \tanh(q_{h1} d_{\mathrm{F1}}), \\
M_{10,8} &= M_{9,8} \cos\alpha, \quad M_{11,8} = M_{9,8} \sin\alpha, \\
M_{10,9} &= -M_{9,9} \cos\alpha, \quad M_{11,9} = -M_{9,9} \sin\alpha.
\end{aligned} \tag{A16}$$

In the above relations, complex conjugation affects only q_{h1} and q_{h2}, since all other parameters entering the expressions are real. All the elements of $\hat{M}$ not mentioned in Eqs. (A16) are equal to zero.

According to the procedure discussed above, the W function can be found explicitly with the help of the $\hat{M}$ matrix.

[1] L. B. Ioffe, V. B. Geshkenbein, M. V. Feigel'man, A. L. Fauchere, and G. Blatter, Nature **398**, 679 (1999)

[2] M. V. Feigel'man, Usp. Fiz. Nauk **169**, 917 (1999) [Phys. Usp. **42**, 823 (1999)].

[3] V. V. Ryazanov, Usp. Fiz. Nauk **169**, 920 (1999) [Phys. Usp. **42**, 825 (1999)].

[4] V. V. Ryazanov, V. A. Oboznov, A. V. Veretennikov, and A. Yu. Rusanov, Phys. Rev. B **65**, 020501(R) (2001).

[5] A. V. Veretennikov, V. V. Ryazanov, V. A. Oboznov, A. Yu. Rusanov, V. A. Larkin, and J. Aarts, Physica B **284-288**, 495 (2000).

[6] V. V. Ryazanov, V. A. Oboznov, A. Yu. Rusanov, A. V. Veretennikov, A. A. Golubov, and J. Aarts, Phys. Rev. Lett. **86**, 2427 (2001).

[7] T. Kontos, M. Aprili, J. Lesueur, F. Genêt, B. Stephanidis, and R. Boursier, Phys. Rev. Lett. **89**, 137007 (2002).

[8] V. V. Ryazanov, V. A. Oboznov, V. V. Bol'ginov, A. S. Prokof'ev, and A. K. Feofanov, Usp. Fiz. Nauk **174**, 795 (2004) [Phys. Usp. **47**, 732 (2004)].

[9] S. Oh, D. Youm, and M. R. Beasley, Appl. Phys. Lett. **71**, 2376 (1997).

[10] L. R. Tagirov, Phys. Rev. Lett. **83**, 2058 (1999).

[11] P. V. Leksin, N. N. Garif'yanov, I. A. Garifullin, J. Schumann, H. Vinzelberg, V. Kataev, R. Klingeler, O. G. Schmidt, and B. Büchner, Appl. Phys. Lett. **97**, 102505 (2010).

[12] Ya. V. Fominov, A. A. Golubov, T. Yu. Karminskaya, M. Yu. Kupriyanov, R. G. Deminov, and L. R. Tagirov, Pis'ma Zh. Eksp. Teor. Fiz. **91**, 329 (2010) [JETP Lett. **91**, 308 (2010)].

[13] P. V. Leksin, N. N. Garif'yanov, I. A. Garifullin, J. Schumann, V. Kataev, O. G. Schmidt, and B. Büchner, Phys. Rev. Lett. **106**, 067005 (2011).

[14] I. A. Garifullin, P. V. Leksin, N. N. Garif'yanov, A. A. Kamashev, Ya. V. Fominov, J. Schumann, Y. Krupskaya, V. Kataev, O. G. Schmidt, and B. Büchner, J. Magn. Magn. Mater. **373**, 18 (2015).

[15] M. G. Blamire and J. W. A. Robinson, J. Phys.: Condens. Matter **26**, 453201 (2014).

[16] J. Linder and J. W. A. Robinson, Nat. Phys. **11**, 307 (2015).

[17] N. G. Pugach, M. Safonchik, T. Champel, M. E. Zhitomirsky, E. Lähderanta, M. Eschrig, and C. Lacroix, Appl. Phys. Lett. **111**, 162601 (2017).

[18] Q. Cheng and B. Jin, Physica C **473**, 29 (2012).

[19] J. Zhu, I. N. Krivorotov, K. Halterman, and O. T. Valls, Phys. Rev. Lett. **105**, 207002 (2010).

[20] F. S. Bergeret, A. F. Volkov, and K. B. Efetov, Rev. Mod. Phys. **77**, 1321 (2005).

[21] C. T. Wu and O. T. Valls, J. Supercond. Nov. Magn. **25**, 2173 (2012).

[22] V. I. Zdravkov, J. Kehrle, G. Obermeier, D. Lenk, H.-A. Krug von Nidda, C. Müller, M. Yu. Kupriyanov, A. S. Sidorenko,

S. Horn, R. Tidecks, and L. R. Tagirov, Phys. Rev. B **87**, 144507 (2013).
[23] N. Banerjee, C. B. Smiet, R. G. J. Smits, A. Ozaeta, F. S. Bergeret, M. G. Blamire, and J. W. A. Robinson, Nat. Commun. **5**, 3048 (2014).
[24] X. L. Wang, A. Di Bernardo, N. Banerjee, A. Wells, F. S. Bergeret, M. G. Blamire, and J. W. A. Robinson, Phys. Rev. B **89**, 140508(R) (2014).
[25] M. G. Flokstra, T. C. Cunningham, J. Kim, N. Satchell, G. Burnell, P. J. Curran, S. J. Bending, C. J. Kinane, J. F. K. Cooper, S. Langridge, A. Isidori, N. Pugach, M. Eschrig, and S. L. Lee, Phys. Rev. B **91**, 060501(R) (2015).
[26] K. Dybko, P. Aleshkevych, M. Sawicki, and P. Przyslupski, J. Magn. Magn. Mater. **373**, 48 (2015).
[27] D. Lenk, V. I. Zdravkov, J.-M. Kehrle, G. Obermeier, A. Ullrich, R. Morari, H.-A. Krug von Nidda, C. Müller, M. Yu. Kupriyanov, A. S. Sidorenko, S. Horn, R. G. Deminov, L. R. Tagirov, and R. Tidecks, Beilstein J. Nanotechnol. **7**, 957 (2016).
[28] S. Voltan, A. Singh, and J. Aarts, Phys. Rev. B **94**, 054503 (2016).
[29] Z. Feng, J. W. A. Robinson, and M. G. Blamire, Appl. Phys. Lett. **111**, 042602 (2017).
[30] A. Srivastava, L. A. B. Olde Olthof, A. Di Bernardo, S. Komori, M. Amado, C. Palomares-Garcia, M. Alidoust, K. Halterman, M. G. Blamire, and J. W. A. Robinson, Phys. Rev. Appl. **8**, 044008 (2017).
[31] E. Moen and O. T. Valls, Phys. Rev. B **95**, 054503 (2017).
[32] Zh. Devizorova and S. Mironov, Phys. Rev. B **95**, 144514 (2017).
[33] M. Alidoust and K. Halterman, Phys. Rev. B **97**, 064517 (2018).
[34] A. A. Jara, C. Safranski, I. N. Krivorotov, C. T. Wu, A. N. Malmi-Kakkada, O. T. Valls, and K. Halterman, Phys. Rev. B **89**, 184502 (2014).
[35] C. T. Wu, O. T. Valls, and K. Halterman, Phys. Rev. B **86**, 014523 (2012).
[36] P. V. Leksin, N. N. Garif'yanov, A. A. Kamashev, A. A. Validov, Ya. V. Fominov, J. Schumann, V. Kataev, J. Thomas, B. Büchner, and I. A. Garifullin, Phys. Rev. B **93**, 100502(R) (2016).
[37] J. Y. Gu, C.-Y. You, J. S. Jiang, J. Pearson, Y. B. Bazaliy, and S. D. Bader, Phys. Rev. Lett. **89**, 267001 (2002).
[38] Y. Gu, G. B. Halász, J. W. A. Robinson, and M. G. Blamire, Phys. Rev. Lett. **115**, 067201 (2015).
[39] A. Singh, S. Voltan, K. Lahabi, and J. Aarts, Phys. Rev. X **5**, 021019 (2015).
[40] A. A. Kamashev, P. V. Leksin, J. Schumann, V. Kataev, J. Thomas, T. Gemming, B. Büchner, and I. A. Garifullin, Phys. Rev. B **96**, 024512 (2017).
[41] A. A. Kamashev, P. V. Leksin, N. N. Garif'yanov, A. A. Validov, J. Schumann, V. Kataev, B. Büchner, and I. A. Garifullin, J. Magn. Magn. Mater. **459**, 7 (2018).
[42] A. A. Kamashev, N. N. Garif'yanov, A. A. Validov, J. Schumann, V. Kataev, B. Büchner, Ya. V. Fominov, and I. A. Garifullin, Beilstein J. Nanotechnol. **10**, 1458 (2019).
[43] P. V. Leksin, N. N. Garif'yanov, A. A. Kamashev, Ya. V. Fominov, J. Schumann, C. Hess, V. Kataev, B. Büchner, and I. A. Garifullin, Phys. Rev. B **91**, 214508 (2015).
[44] P. V. Leksin, A. A. Kamashev, J. Schumann, V. E. Kataev, J. Thomas, B. Büchner, and I. A. Garifullin, Nano Res. **9**, 1005 (2016).
[45] S. Husain, S. Akansel, A. Kumar, P. Svedlindh, and S. Chaudhary, Sci. Rep. **6**, 28692 (2016).
[46] C. Kittel, *Introduction to Solid State Physics* (Willey, New York, 1976).
[47] A. Pippard, Rep. Prog. Phys. **23**, 176 (1960).
[48] Y. V. Kudryavtsev, V. N. Uvarov, V. A. Oksenenko, Y. P. Lee, J. B. Kim, Y. H. Hyun, K. W. Kim, J. Y. Rhee, and J. Dubowik, Phys. Rev. B **77**, 195104 (2008).
[49] N. I. Kourov, A. V. Korolev, N. V. Marchenkov, A. V. Lukojanov, and K. A. Belozerova, Fiz. Tverd. Tela **55**, 899 (2013) [Phys. Sol. State **55**, 977 (2013)].
[50] Ya. V. Fominov, N. M. Chtchelkatchev, and A. A. Golubov, Phys. Rev. B **66**, 014507 (2002).
[51] M. Yu. Kuprianov and V. F. Lukichev, Zh. Eksp. Teor. Fiz. **94**, 139 (1988) [Sov. Phys. JETP **67**, 1163 (1988)].
[52] P. V. Leksin, N. N. Garif'yanov, I. A. Garifullin, Ya. V. Fominov, J. Schumann, Y. Krupskaya, V. Kataev, O. G. Schmidt, and B. Büchner, Phys. Rev. Lett. **109**, 057005 (2012).
[53] K. D. Usadel, Phys. Rev. Lett. **25**, 507 (1970).
[54] R. G. Deminov, L. R. Tagirov, R. R. Gaifullin, T. Yu. Karminskaya, M. Yu. Kupriyanov, Ya. V. Fominov, and A. A. Golubov, J. Magn. Magn. Mater. **373**, 16 (2015); R. G. Deminov, L. R. Tagirov, R. R. Gaifullin, Ya. V. Fominov, T. Yu. Karminskaya, M. Yu. Kupriyanov, and A. A. Golubov, Solid State Phenom. **233-234**, 745 (2015).
[55] M. Avdeev and Yu. Proshin, J. Low Temp. Phys. **185**, 453 (2016).
[56] S. Mironov and A. Buzdin, Phys. Rev. B **92**, 184506 (2015).
[57] K. Halterman and M. Alidoust, Phys. Rev. B **94**, 064503 (2016).
[58] D. A. Ivanov and Ya. V. Fominov, Phys. Rev. B **73**, 214524 (2006).
[59] Ya. V. Fominov, N. M. Chtchelkatchev, and A. A. Golubov, Pis'ma Zh. Eksp. Teor. Fiz. **74**, 101 (2001) [JETP Lett. **74**, 96 (2001)].